AMERICAN SOCIETY FOR MICROBIOLOGY | Journal of Virology®

PATHOGENESIS AND IMMUNITY

Contribution of SARS-CoV-2 Accessory Proteins to Viral Pathogenicity in K18 Human ACE2 Transgenic Mice

Jesus A. Silvas,[a] Desarey Morales Vasquez,[a] Jun-Gyu Park,[a] Kevin Chiem,[a] Anna Allué-Guardia,[a] Andreu Garcia-Vilanova,[a] Roy Neal Platt,[a] Lisa Miorin,[b,c] Thomas Kehrer,[b,c,d] Anastasija Cupic,[b,c] Ana S. Gonzalez-Reiche,[e] Harm van Bakel,[e] Adolfo García-Sastre,[b,c,f,g] Tim Anderson,[a] Jordi B. Torrelles,[a] Chengjin Ye,[a] Luis Martinez-Sobrido[a]

[a]Texas Biomedical Research Institute, San Antonio, Texas, USA
[b]Department of Microbiology, Icahn School of Medicine at Mount Sinai, New York, New York, USA
[c]Global Health Emerging Pathogens Institute, Icahn School of Medicine at Mount Sinai, New York, New York, USA
[d]Graduate School of Biomedical Sciences, Icahn School of Medicine at Mount Sinai, New York, New York, USA
[e]Department of Genetics and Genomic Sciences, Icahn School of Medicine at Mount Sinai, New York, New York, USA
[f]Department of Medicine, Division of Infectious Diseases, Icahn School of Medicine at Mount Sinai, New York, New York, USA
[g]Tisch Cancer Institute, Icahn School of Medicine at Mount Sinai, New York, New York, USA

ABSTRACT Severe acute respiratory syndrome coronavirus 2 (SARS-CoV-2) is the viral pathogen responsible for the current coronavirus disease 2019 (COVID-19) pandemic. As of 19 May 2021, John Hopkins University's COVID-19 tracking platform reported 3.3 million deaths associated with SARS-CoV-2 infection. Currently, the World Health Organization has granted emergency use listing (EUL) to six COVID-19 vaccine candidates. However, much of the pathogenesis observed during SARS-CoV-2 infection remains elusive. To gain insight into the contribution of individual accessory open reading frame (ORF) proteins in SARS-CoV-2 pathogenesis, we used our recently described reverse-genetics system approach to successfully engineer recombinant SARS-CoV-2 (rSARS-CoV-2) constructs; we removed individual viral ORF3a, −6, −7a, −7b, and −8 proteins from them, and we characterized the resulting recombinant viruses *in vitro* and *in vivo*. Our results indicate differences in plaque morphology, with ORF-deficient (ΔORF) viruses producing smaller plaques than those of the wild type (rSARS-CoV-2/WT). However, growth kinetics of ΔORF viruses were like those of rSARS-CoV-2/WT. Interestingly, infection of K18 human angiotensin-converting enzyme 2 (hACE2) transgenic mice with the ΔORF rSARS-CoV-2s identified ORF3a and ORF6 as the major contributors of viral pathogenesis, while ΔORF7a, ΔORF7b, and ΔORF8 rSARS-CoV-2s induced pathology comparable to that of rSARS-CoV-2/WT. This study demonstrates the robustness of our reverse-genetics system to generate rSARS-CoV-2 constructs and the major role for ORF3a and ORF6 in viral pathogenesis, providing important information for the generation of attenuated forms of SARS-CoV-2 for their implementation as live attenuated vaccines for the treatment of SARS-CoV-2 infection and associated COVID-19.

IMPORTANCE Despite great efforts put forward worldwide to combat the current coronavirus disease 2019 (COVID-19) pandemic, severe acute respiratory syndrome coronavirus 2 (SARS-CoV-2) continues to be a human health and socioeconomic threat. Insights into the pathogenesis of SARS-CoV-2 and the contribution of viral proteins to disease outcome remain elusive. Our study aims (i) to determine the contribution of SARS-CoV-2 accessory open reading frame (ORF) proteins to viral pathogenesis and disease outcome and (ii) to develop a synergistic platform combining our robust reverse-genetics system to generate recombinant SARS-CoV-2 constructs with a validated rodent model of infection and disease. We demonstrate that SARS-CoV-2 ORF3a and ORF6 contribute to lung pathology and ultimately disease outcome in K18 hACE2 transgenic mice, while ORF7a, ORF7b, and ORF8 have little impact on disease outcome. Moreover, our combinatory platform serves as a foundation for

Citation Silvas JA, Vasquez DM, Park J-G, Chiem K, Allué-Guardia A, Garcia-Vilanova A, Platt RN, Miorin L, Kehrer T, Cupic A, Gonzalez-Reiche AS, Bakel HV, García-Sastre A, Anderson T, Torrelles JB, Ye C, Martinez-Sobrido L. 2021. Contribution of SARS-CoV-2 accessory proteins to viral pathogenicity in K18 human ACE2 transgenic mice. J Virol 95:e00402-21. https://doi.org/10.1128/JVI.00402-21.

Editor Colin R. Parrish, Cornell University

Address correspondence to Chengjin Ye, cye@txbiomed.org, or Luis Martinez-Sobrido, lmartinez@txbiomed.org.

We dedicate this paper to all COVID-19 victims and to all heroes battling this disease.

Received 7 March 2021
Accepted 3 June 2021
Accepted manuscript posted online 16 June 2021
Published 10 August 2021

generating attenuated forms of the virus to develop live attenuated vaccines for the treatment of SARS-CoV-2.

KEYWORDS SARS-CoV-2, COVID-19, K18 hACE2 transgenic mice, ORF3a, ORF6, ORF7a, ORF7b, ORF8, hACE2, pathogenesis

Coronaviruses (CoVs) are enveloped, positive-sense, single-stranded RNA viruses that cause both mild and lethal upper respiratory illness in humans (1–3). Highly pathogenic and lethal severe acute respiratory syndrome (SARS) and Middle Eastern respiratory syndrome (MERS) CoVs were first identified in early 2000 and 2010 as spillover events to humans from horseshoe bats and dromedary camels, respectively (2, 4, 5). In December 2019, a respiratory infectious disease disseminated throughout the Chinese city of Wuhan, and by the spring of 2020, it had spread worldwide (6). A novel coronavirus, SARS-CoV-2, was identified as the etiological agent of the new coronavirus disease 2019 (COVID-19) pandemic (6–8).

The SARS-CoV-2 genome encodes 16 nonstructural proteins (NSPs) and 6 accessory proteins, each encoded by independent open reading frames (ORFs) (9). It has been described that both coronavirus NSP and ORF proteins play important roles in viral replication and transcription, evasion of host immune responses, and viral dissemination (10, 11). In particular, SARS-CoV ORF3a has been implicated as an inducer of membrane rearrangement and cell death (12–14). SARS-CoV ORF3b, ORF6, and nucleocapsid (N) proteins have been described to counteract the host immune interferon (IFN) responses (15). Moreover, SARS-CoV ORF7a protein has also been shown to inhibit cellular protein synthesis and activation of p38 mitogen-activated protein kinase (16). Conversely, coronavirus ORF7b has been reported to have a Golgi localization signal, where it becomes incorporated into the virion; however, no additional studies have delved into any further functions (17, 18). Furthermore, with regard to SARS-CoV-2, early clinical isolates identified a 382-nucleotide deletion leading to a truncated ORF7b protein and removal of the ORF8 transcription signal (19). Lastly, SARS-CoV-2 ORF8 has been postulated to play a minor role in disease outcome, as natural SARS-CoV-2 strains containing deletions in ORF8 have been isolated from individuals presenting with COVID-19 (20). Nevertheless, only a limited number of studies have examined the contribution of coronavirus NSP or ORF proteins to pathogenesis and disease outcome in animal models of infection.

To examine the contribution of accessory proteins in the pathogenicity of SARS-CoV-2, we used our previously described reverse-genetics approach based on the use of a bacterial artificial chromosome (BAC) to rescue recombinant SARS-CoV-2 (rSARS-CoV-2) with deletions of individual accessory ORF proteins (21). We were able to successfully rescue rSARS-CoV-2 constructs deficient in ORF3a, ORF6, ORF7a, ORF7b, and ORF8 individually. The *in vitro* characterization of each deficient-ORF (ΔORF) virus revealed a distinct difference in plaque phenotype from that of the recombinant wild-type SARS-CoV-2 (rSARS-CoV-2/WT). This phenotypic change, however, did not affect the viral growth kinetics, since all ΔORF rSARS-CoV-2s replicated similarly to the rSARS-CoV-2/WT. Interestingly, we observed changes in pathogenesis between the WT and ΔORF rSARS-CoV-2s in the established K18 human angiotensin-converting enzyme 2 (hACE2) transgenic mouse model of SARS-CoV-2 infection (22). In contrast to the WT and the ORFΔ7a, ORFΔ7b, and ORFΔ8 rSARS-CoV-2s, the ORFΔ3a and ORFΔ6 rSARS-CoV-2s induced less pathology and resulted in 75% and 50% survival rates, respectively. Furthermore, both the ORFΔ3a and ORFΔ6 rSARS-CoV-2s had lower viral titers (10^2 PFU/ml) at 2 days postinfection (p.i.) and by 4 days p.i. were no longer detected in nasal turbinates. In contrast, ORFΔ6 viral strain replication in the lungs reached 10^5 PFU/ml at 2 days p.i. and only decreased by $\sim$2 $\log_{10}$ at 4 days p.i. ORFΔ3a virus replication reached only 10^2 PFU/ml at 2 days p.i. and was not detected by 4 days p.i. in the lungs. Both the ORFΔ7a and ORFΔ7b rSARS-CoV-2s induced pathologies similar to that produced by rSARS-CoV-2/WT and resulted in a 25% survival rate. By merging our *in vitro* and *in vivo* data, we have been able to generate insights into the contribution of

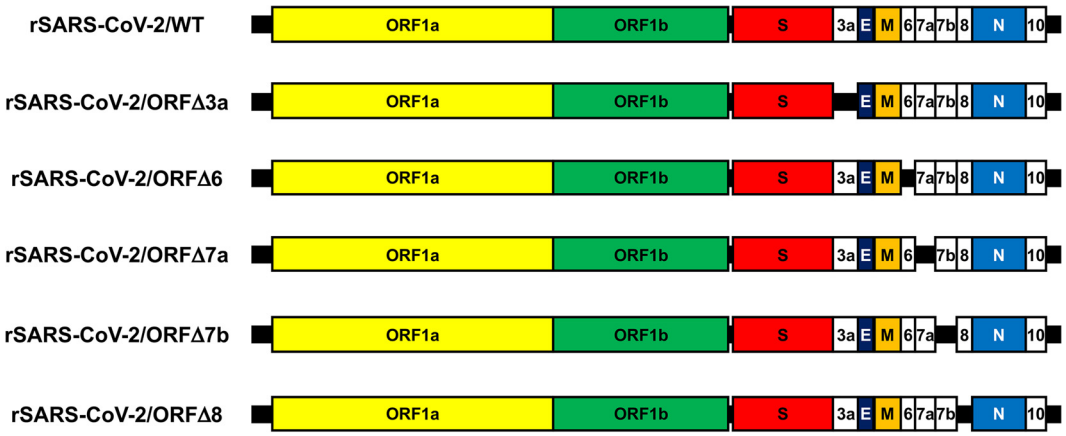

FIG 1 Genome organizations of the WT and ΔORF rSARS-CoV-2s. The SARS-CoV-2 genome includes ~29.8 kb of nucleotides, among which ~21.5 kb encodes the ORF1a and ORF1b replicase. The rest of the ~8.3-kb viral genome encodes the structural spike (S), envelope (E), matrix (M), and nucleocapsid (N) proteins and the accessory ORF3a, −6, −7a, −7b, −8, and −10 proteins. Individual deletions of the ORF accessory proteins were introduced into the BAC for rescue of rSARS-CoV-2. Schematic representations are not drawn to scale.

SARS-CoV-2 accessory ORF proteins in the pathogenesis and disease outcome of SARS-CoV-2 infection. These essential data also pave the way for further designing and developing of live attenuated vaccines against SARS-CoV-2.

RESULTS

Generation of BACs with deletions of individual accessory ORF proteins. The SARS-CoV-2 genome, which was divided into 5 fragments and chemically synthesized, was assembled into a single bacterial artificial chromosome (BAC) that led to efficient virus rescue after transfection into Vero E6 cells using Lipofectamine 2000 (21). Fragment 1 included the SARS-CoV-2 ORF accessory proteins. Using standard gene-engineering approaches, we systematically deleted, individually, ORF3a, ORF6, ORF7a, ORF7b, or ORF8 from fragment 1 using PCR and primer pairs containing BsaI type IIS restriction endonuclease sites. After being confirmed by Sanger sequencing (data not shown), fragment 1 containing the individual deletions of the ORF3a, ORF6, ORF7a, ORF7b, or ORF8 accessory protein were reassembled into the BAC (Fig. 1).

Rescue of ΔORF rSARS-CoV-2s. BACs with individual deletions of an accessory ORF were transfected into Vero E6 cells for the recovery of ΔORF rSARS-CoV-2s, according to our previously described protocol (21). At 72 h posttransfection, tissue culture supernatants (passage 0 [P0]) were collected to inoculate fresh Vero E6 cells (P1). Supernatants were then collected from P1 at 72 h p.i., and viral titers, defined as numbers of PFU per milliliter, were determined as previously described (21). To verify the rescue of each ΔORF rSARS-CoV-2, indirect immunofluorescence was performed using antibodies directed at the nucleocapsid (N) and spike (S) proteins (Fig. 2A). We next verified the individual deletion of each ORF from rSARS-CoV-2 using reverse transcription-PCR (RT-PCR) procedures to amplify the viral N gene (control) and the regions which cover the corresponding individual ORF deletions (Fig. 2B). All the ΔORF rSARS-CoV-2s and rSARS-CoV-2/WT produced an RT-PCR product of approximately 1.2 kb corresponding to the N gene, whereas amplified regions that cover the corresponding ORF deletions were smaller in the ΔORF rSARS-CoV-2 constructs than in rSARS-CoV-2/WT (Fig. 2B), demonstrating the deletion of the individual ORFs from the viral genomes. Individual deletions of the viral proteins from the ΔORF rSARS-CoV-2s were further confirmed by Sanger sequencing of PCR products (Fig. 2C) and deep sequencing analysis of the entire viral genome (Fig. 3). These data demonstrate that each ΔORF rSARS-CoV-2 construct contained a deletion of its individual ORF accessory protein.

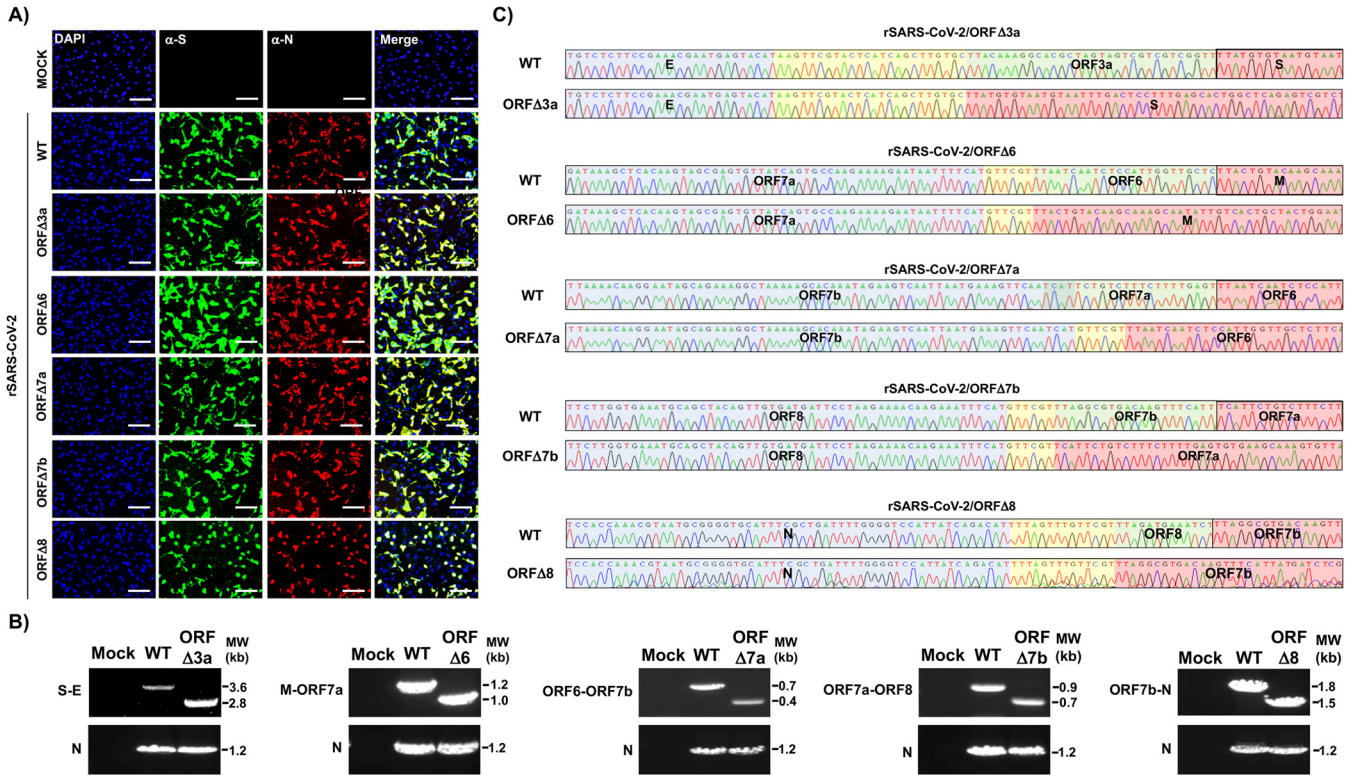

FIG 2 Rescue of ΔORF rSARS-CoV-2. (A) IFA. Vero E6 cells (24-well plate format, 10^5 cells/well, triplicates) were mock infected or infected (MOI of 3) with the WT or the ORFΔ3a, ORFΔ6, ORFΔ7a, ORFΔ7b, or ORFΔ8 rSARS-CoV-2. At 24 h p.i., cells were fixed and immunostained with a cross-reactive polyclonal antibody against SARS-CoV N protein and a cross-reactive monoclonal antibody against SARS-CoV S protein (3B4). Rhodamine red goat anti-rabbit and FITC rabbit anti-mouse secondary antibodies were used, and nuclei were visualized with DAPI. Scale bars, 100 μm. (B) RT-PCR. Vero E6 cells (6-well plate format, 10^6 cells/well) were mock infected or infected (MOI of 0.1) with the WT or a ΔORF rSARS-CoV-2, and total RNA was extracted at 24 h p.i. Regions in the viral genome corresponding with the deletion were amplified, and the N gene was amplified as an internal control. All the products were separated on a 0.8% agarose gel. MW, molecular weight. (C) Sequencing. RT-PCR products from panel B were gel purified and subjected to Sanger sequencing. The consensus sequences in the genomes of both the WT and a ΔORF rSARS-CoV-2 downstream of the deleted gene are indicated in blue, the intergenic regions between viral genes are shown in yellow, the genes deleted from the ΔORF rSARS-CoV-2s are indicated in green, and the viral genes upstream of the deleted ORFs in the rSARS-CoV-2s are shown in red.

Characterization of the ΔORF rSARS-CoV-2 constructs *in vitro*. We next proceeded to characterize each ΔORF rSARS-CoV-2 construct *in vitro* (Fig. 4). Previous studies have shown that manipulation of the viral genome can affect the phenotypes of viral plaques; therefore, as an initial step, we proceeded to investigate whether deletion of individual accessory ORFs had an impact on the rSARS-CoV-2 plaque phenotype (23), as some studies have linked changes in plaque phenotype to attenuation or disease outcome (24, 25). Interestingly, we noticed an effect on the plaque phenotypes of all ΔORF rSARS-CoV-2 constructs compared to that on rSARS-CoV-2/WT at all times p.i. studied (24, 48, 72, and 96 h) (Fig. 4A). We further confirmed these results by measuring the diameters of the plaques of the WT and ORF-deficient rSARS-CoV-2s on Vero E6 cell monolayers (Fig. 4B). Except for ORFΔ7b rSARS-CoV-2, all the other ORF-deficient rSARS-CoV-2s had smaller plaque phenotypes than WT rSARS-CoV-2 at any of the studied time points (Fig. 4A and B). Next, we compared the growth kinetics of the ΔORF rSARS-CoV-2s to that of rSARS-CoV-2/WT in Vero E6 cells. To this end, viral titers in the tissue culture supernatants from Vero E6 cells infected (multiplicity of infection [MOI], 0.01) with the WT or ΔORF rSARS-CoV-2 collected at 12, 24, 48, 72, and 96 h p.i. were determined by plaque assay (Fig. 4C). No statistically significant differences between the WT and ORFΔ3a, ORFΔ6, and ORFΔ7b rSARS-CoV-2s were observed at any times p.i., except for the replication of ORFΔ7a and ORFΔ8 rSARS-CoV-2s, which was significantly different (~1 $\log_{10}$) than that of rSARS-CoV-2/WT at 12 and 24 h p.i. (Fig. 4C). Peak viral titers for all ΔORF rSARS-CoV-2s and rSARS-CoV-2/WT were observed between 24 and 48 h p.i., with viral titers decreasing (~1 $\log_{10}$) at later times

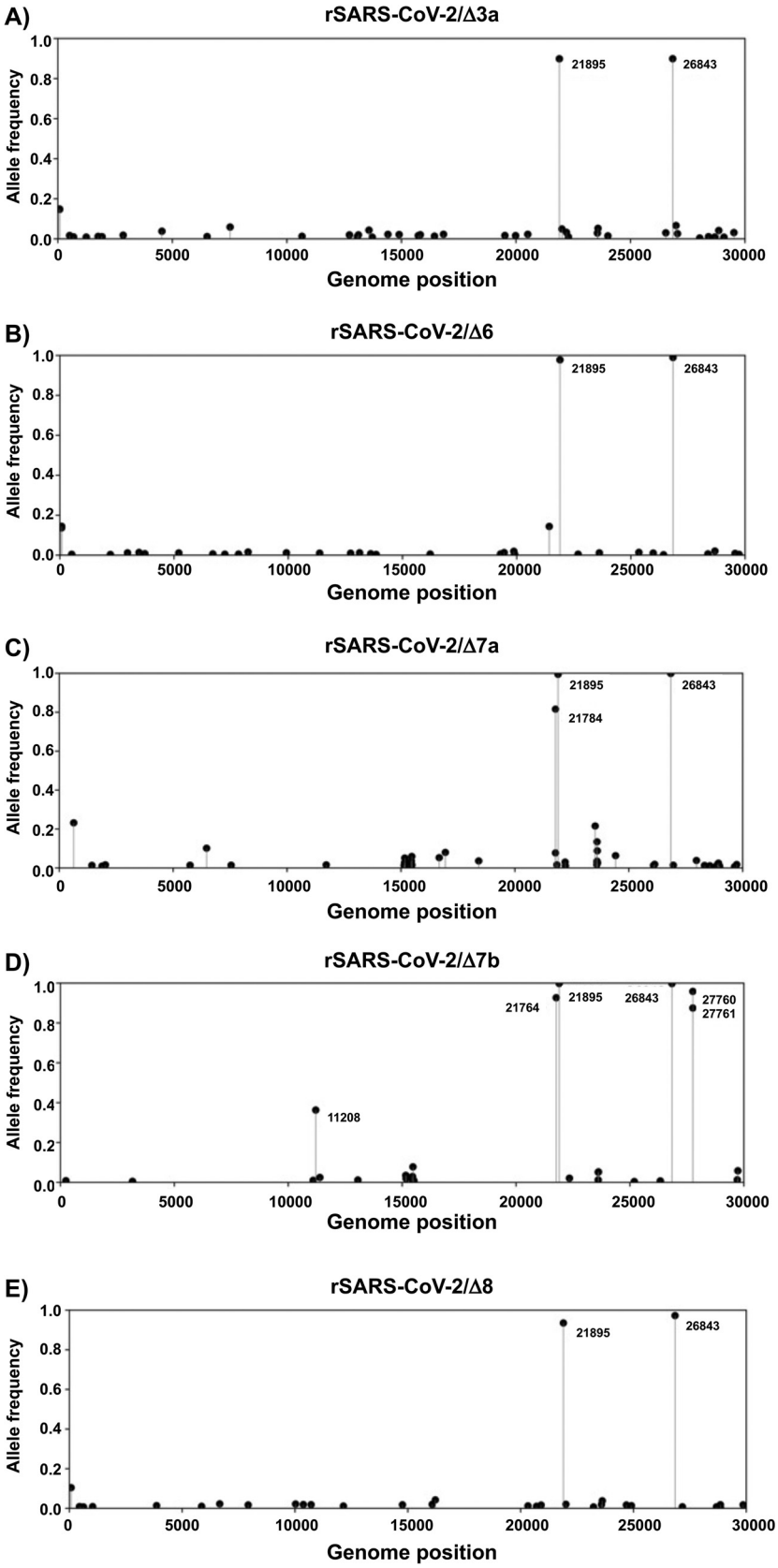

FIG 3 Deep sequencing analysis of ORF-deficient rSARS-CoV-2s. The ORF-deficient rSARS-CoV-2 nonreference allele frequency was calculated by comparing short reads to the sequence of the

(Continued on next page)

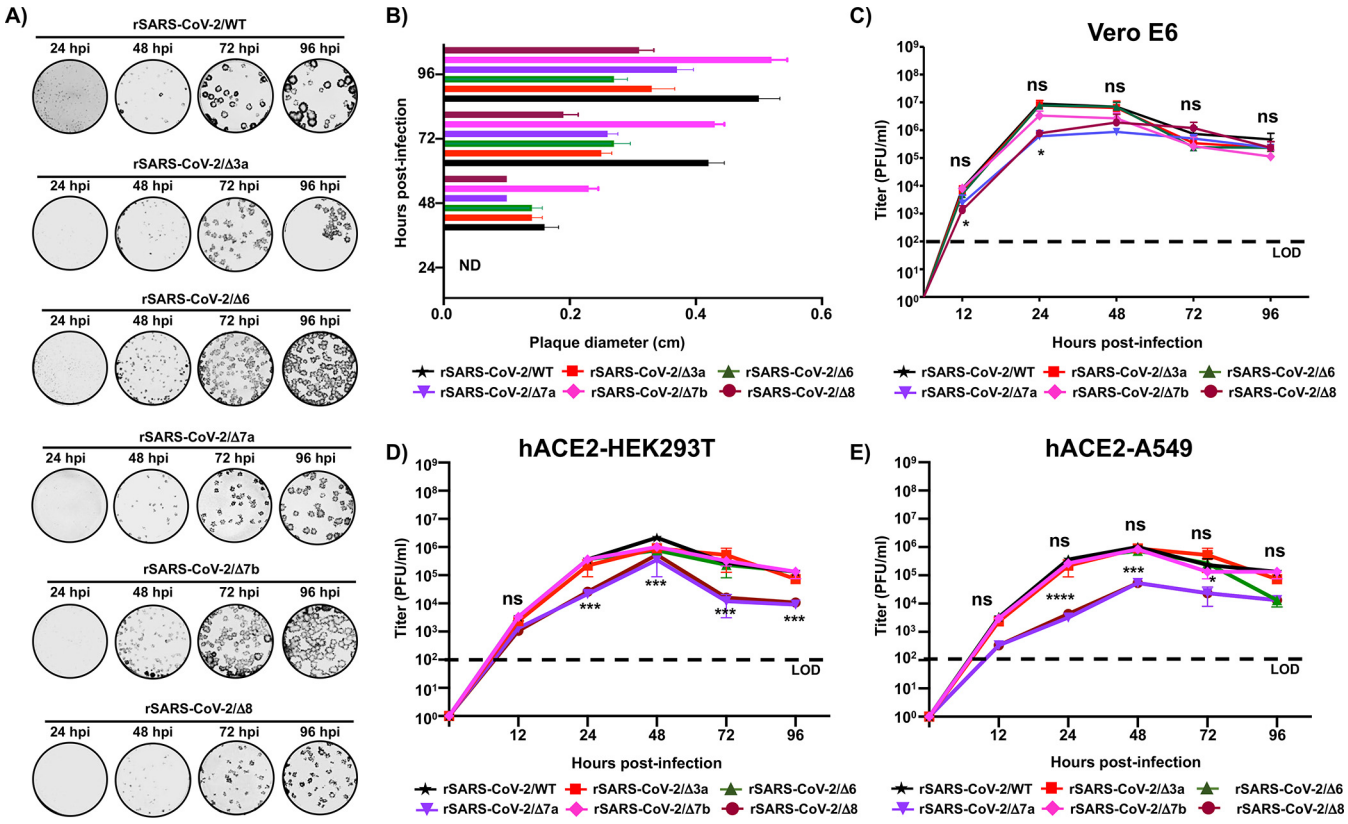

FIG 4 *In vitro* characterization of the WT and ΔORF rSARS-CoV-2s. (A) Plaque phenotype. Vero E6 cells (6-well plate format, 10^6 cells/well) were infected with the WT, ORFΔ3a, ORFΔ6, ORFΔ7a, ORFΔ7b, or ORFΔ8 rSARS-CoV-2 and overlaid with medium containing agar. Plates were incubated at 37°C, and monolayers were immunostained with an anti-N protein SARS-CoV cross-reactive monoclonal antibody, 1C7C7, at the indicated hours p.i. (B) Viral plaque sizes. Diameters of viral plaques were measured with a ruler in centimeters. Plaques less than 0.1 cm are indicated as not detected (ND). (C to E) Multicycle growth kinetics. Vero E6 (C), hACE2-HEK293T (D), and hACE2-A549 (E) cells (6-well plate format, 10^6 cells/well, triplicates) were infected (MOI 0.01) with the WT or a ΔORF rSARS-CoV-2 and incubated at 37°C. At the indicated hours p.i., tissue culture supernatants from infected cells were collected, viral titers were determined by plaque assay (PFU per milliliter), and cells were immunostained using the anti-N SARS-CoV cross-reactive monoclonal antibody 1C7C7. Data are the means ± standard deviations (SDs) of the results determined from triplicate wells. Dotted black lines indicate the limit of detection (LOD; 100 PFU/ml). *, $P < 0.05$, using the Student *t* test. ns, not significant.

p.i., consistent with previous studies with SARS-CoV-2 natural isolates (26, 27). To further assess the effect of ORF deletions on viral fitness and replication, we determined growth kinetics in human HEK293T and A549 cells stably expressing the hACE2 receptor (hACE2-HEK293T and hACE2-A549 cells, respectively), which have been shown to be permissive to SARS-CoV-2 infection (28, 29). We observed that in hACE2-HEK293T (Fig. 4D) and hACE2-A549 (Fig. 4E) cells, the WT and ORF-deficient rSARS-CoV-2 infections peaked at 48 h p.i. and began to decrease at the latter time points, a trend similar to what we observed in Vero E6 cells (Fig. 4C). However, in contrast to the WT and other ORF-deficient rSARS-CoV-2s, both the ORFΔ7a and ORFΔ8 rSARS-CoV-2s replicated significantly less after 12 h p.i. Moreover, we observed a decrease in ORFΔ6 rSARS-CoV-2 titers after the peak at 48 h p.i. All together, these results suggest that despite slight differences in plaque phenotype, ΔORF rSARS-CoV-2s have replication kinetics similar to that of rSARS-CoV-2/WT in Vero E6 cells, while the ORFΔ7a, ORFΔ8, and ORFΔ6 rSARS-CoV-2s have altered replication capabilities in human cell lines, especially in hACE2-A549 cells, which are competent in innate immune responses.

Characterization of ΔORF rSARS-CoV-2s *in vivo*. Coronavirus ORF accessory proteins have been implicated as virulence factors and contribute to both pathogenicity

FIG 3 Legend (Continued)
respective reference WT SARS-CoV-2 USA-WA1/2020 strain genome. Silent mutations at positions 21895 and 26843 (according to the genome positions of the USA-WA1/2020 strain) were fixed in all ORF-deficient rSARS-CoV-2 genomes (21).

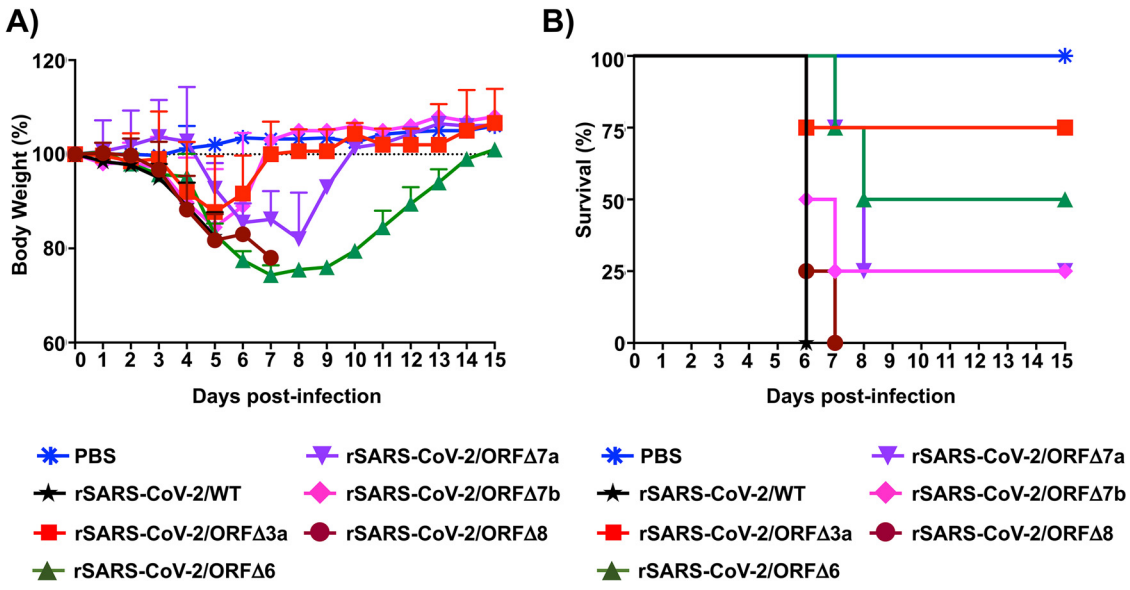

FIG 5 Infection of K18 hACE2 transgenic mice with the WT or a ΔORF rSARS-CoV-2. Six- to 8-week-old K18 hACE2 transgenic female mice were mock (PBS) infected or infected (i.n.) with 10^5 PFU of the WT or a ΔORF rSARS-CoV-2 ($n = 4$/group). Body weight (A) and survival (B) were evaluated at the indicated days p.i. Mice that lost >25% of their initial body weight were humanely euthanized. Error bars represent the SDs of the mean for each group.

and disease outcome (12, 13, 20, 30–32). Therefore, we proceeded to further investigate the contribution of SARS-CoV-2 ORF3a, ORF6, ORF7a, ORF7b, and ORF8 to viral pathogenicity and disease outcome in our previously established K18 hACE2 transgenic mouse model of SARS-CoV-2 infection and COVID-19 disease (22). Four- to 6-week-old female mice ($n = 4$) were mock (phosphate-buffered saline [PBS]) infected or infected (10^5 PFU) with rSARS-CoV-2/WT or with one of the ΔORF rSARS-CoV-2s and observed for 14 days for morbidity (body weight loss) and mortality (survival) (Fig. 5). Our results indicate similar decreases in body weight percentages up to 5 days p.i., from which ORFΔ3a and ORFΔ7b rSARS-CoV-2-infected mice began to recover (Fig. 5A). Interestingly, mice infected with ORFΔ6 and ORFΔ7a rSARS-CoV-2s continued to lose body weight until 7 and 8 days p.i., respectively, and to start to recover (Fig. 5A). All mice infected with the WT or ORFΔ8 rSARS-CoV-2 succumbed to viral infection by 6 or 7 days p.i., respectively (Fig. 5B). Our continued observations of mice infected with ORFΔ3a, ORFΔ6a, ORFΔ7a, and ORFΔ7b rSARS-CoV-2s identified survival rates of 75%, 50%, 25%, and 25%, respectively (Fig. 5B). Upon full comparison, it is worth noting that despite the early onset of morbidity observed in mice infected with the ORFΔ3a rSARS-CoV-2, 3 out of 4 mice survived viral infection, suggesting that ORF3a may play an important role in viral pathogenesis. This early onset of morbidity and quick recovery may be the result of an active immune response to viral infection and, therefore, viral clearance.

We next evaluated viral replication in nasal turbinates and lungs of K18 hACE2 transgenic mice infected with the WT or ΔORF rSARS-CoV-2 at 2 and 4 days p.i. (Fig. 6). At 2 days p.i., the WT and ORFΔ6 rSARS-CoV-2 were detected in nasal turbinates in all mice, with rSARS-CoV-2/WT reaching titers of up to 5×10^3 PFU/ml, while ORFΔ6 rSARS-CoV-2 peaked at 5×10^2 PFU/ml. We detected ORFΔ3a rSARS-CoV-2 (10^2 PFU/ml) in only 50% of infected mice, while ORFΔ7b rSARS-CoV-2 replicated up to 3×10^3 PFU/ml in 75% of infected mice. Only 50% of mice had detectable levels (ranging between 0.5×10^3 and 1×10^3 PFU/ml) of ORFΔ8 rSARS-CoV-2 (Fig. 6A). Interestingly, out of all the ΔORF rSARS-CoV-2s tested, ORFΔ7a replicated in the nasal turbinate to levels (5×10^4 PFU/ml) higher than those observed with rSARS-CoV-2/WT. By 4 days p.i., ORFΔ3a and ORFΔ6 rSARS-CoV-2s were no longer detected in nasal turbinates, while

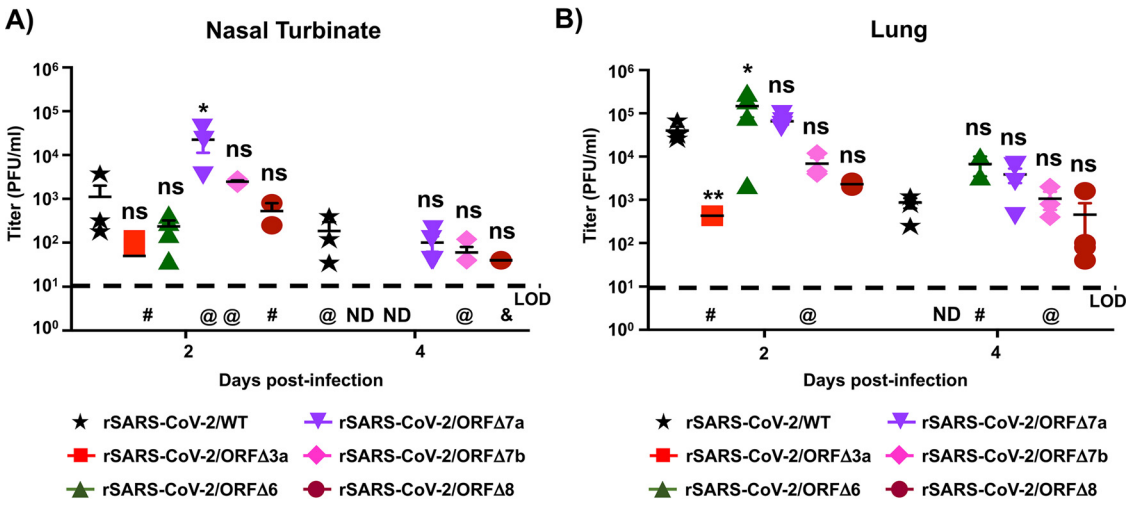

FIG 6 Replication of the WT and ΔORF rSARS-CoV-2s in nasal turbinate and lungs. Six- to 8-week-old K18 hACE2 transgenic female mice were mock (PBS) infected or infected (i.n.) with 10^5 PFU of the WT or a ΔORF rSARS-CoV-2 ($n = 8$/group). Mice were sacrificed at 2 ($n = 4$/group) and 4 ($n = 4$/group) days p.i., and viral titers in nasal turbinate and lung were determined by plaque assay (PFU per milliliter) and immunostaining using the cross-reactive SARS-CoV 1C7C7 N protein monoclonal antibody. Viral titers in the nasal turbinate (A) and lungs (B) are shown. Symbols represent data from individual mice and bars the geometric means of viral titers. Dotted lines indicate the LOD (10 PFU/ml). ND, not detected; @, not detected in 1 mouse; #, not detected in 2 mice: &, not detected in 3 mice. Negative results of the PBS-infected mice are not plotted.

75% of mice infected with rSARS-CoV-2/WT had viral titers ranging between 5×10^1 and 5×10^2 PFU/ml. ORFΔ7a, ORFΔ7b, and ORFΔ8 rSARS-CoV-2s replicated to lower levels ($\sim 5 \times 10^1$ PFU/ml) than rSARS-CoV-2/WT (Fig. 6A). In the lungs, the WT and ORFΔ6 and ORFΔ7a rSARS-CoV-2s were detected at levels of $\sim 10^5$ PFU/ml at 2 days p.i. (Fig. 6B). Viral titers of ORFΔ7b and ORFΔ8 rSARS-CoV-2s ($\sim 10^4$ PFU/ml) and ORFΔ3a ($\sim 0.5 \times 10^2$ PFU/ml) rSARS-CoV-2 were lower than those of rSARS-CoV-2/WT (Fig. 6B). Interestingly, by 4 days p.i., ORFΔ3a rSARS-CoV-2 was no longer detected in the lungs, while WT, ORFΔ6, ORFΔ7a, ORFΔ7b, and ORFΔ8 rSARS-CoV-2s decreased only ~ 1 $\log_{10}$ to levels observed by 2 days p.i. (Fig. 6B).

Furthermore, to evaluate the impact of viral infection in the lungs of infected animals, we performed gross pathology analysis on lungs collected at 2 and 4 days p.i. (Fig. 7A). Both the WT and ΔORF rSARS-CoV-2s induced similar pathologies at 2 days p.i., with the WT, ORFΔ7a, and ORFΔ7b rSARS-CoV-2s inducing pathological lesions in more than 50% of the lung area (Fig. 7B). Intriguingly, by 4 days p.i., only WT and ORFΔ8 rSARS-CoV-2-infected lungs maintained pathological lesions, while ORFΔ3a, ORFΔ6, ORFΔ7a, and ORFΔ7b rSARS-CoV-2-infected lungs appeared to recover from lesions observed at 2 days p.i. All together, these *in vivo* results provide new insight into the contribution of SARS-CoV-2 accessory ORF proteins in viral pathogenesis and disease, suggesting a major role of ORF3a and ORF6 and a smaller impact of ORF7a, ORF7b, and ORF8 on virulence and disease outcome.

Lastly, we evaluated the induction of chemokines and cytokines during infection in the lung using an 8-plex Luminex assay (Fig. 8). We previously published that infection of K18 hACE2 transgenic mice with the SARS-CoV-2 WA-1/US strain induces local chemokine and cytokine storms in the lung (22). Compared to mock-infected K18 hACE2 transgenic mice, infection of mice with rSARS-CoV-2/WT induced a significant production of type I interferon (IFN-α) and type II IFN (IFN-γ) responses and chemo-attractants (e.g., CCL5/RANTES) at 2 days p.i. (Fig. 8A). However, production of tumor necrosis factor alpha (TNF-α) (TH1), interleukin 6 (IL-6), IL-10 (TH2), and IL-17 (TH17) responses were low in rSARS-CoV-2/WT-infected K18 hACE2 transgenic mice (Fig. 8A). All the ORF-deficient rSARS-CoV-2 constructs induced IFN responses at different levels, and the highest production of IFN-α and CCL5/RANTES was observed in mice infected with

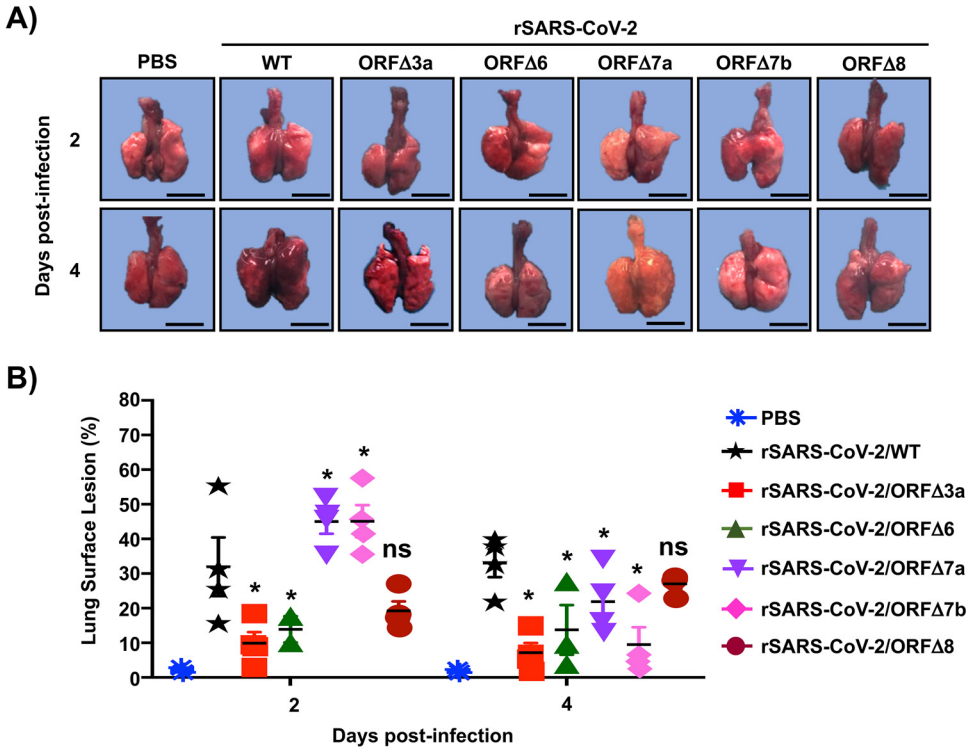

FIG 7 Gross pathology analysis of lungs from K18 hACE2 transgenic mice infected with the WT or a ΔORF rSARS-CoV-2. Lungs from 6-to-8-week-old female K18 hACE2 transgenic mice ($n = 8$/group) mock (PBS) infected or infected (i.n.) with 10^5 PFU of the WT or a ΔORF rSARS-CoV-2 were harvested at 2 ($n = 4$/group) or 4 ($n = 4$/group) days p.i., imaged (A), and scored for virally induced lesions (B). The total lung surface area affected by virally induced lesions were determined. Scale bars, 3 cm.

ΔORF6 rSARS-CoV-2. At 2 days p.i., no significant TH1 and TH2 responses were observed with any of the ORF-deficient rSARS-CoV-2s, except for ΔORF3a SARS-CoV-2, which induced significant levels of IL-10 (TH2). Conversely, elevated TH17 responses were observed for both ΔORF7b and ΔORF8 rSARS-CoV-2s. At 4 days p.i., all immunomodulator levels dropped to become nonsignificant compared to levels in rSARS-CoV-2/WT-infected K18 hACE2 transgenic mice, except for the levels of TNF-α induced by ΔORF7a SARS-CoV-2 infection, which remained significantly elevated. Importantly, when looking at predictors of the cytokine storm outcome (33), the IL-6/IL-10 ratio was lower for ΔORF3a rSARS-CoV-2. Together with ΔORF3a rSARS-CoV-2 inducing early onset of morbidity, less mortality, lower lung viral titers, and less tissue damage, these results indicate a major role for ORF3a in viral pathogenesis. Interestingly, ΔORF8 rSARS-CoV-2 behaved like rSARS-CoV-2/WT (e.g., higher morbidity/mortality and viral titers), and as such, this mutant virus also presented the highest IL-6/IL-10 ratio at 2 days p.i. (Fig. 8B). As expected, the IL-6/IL-10 ratio became normalized across all rSARS-CoV-2 constructs evaluated by 4 days p.i. (Fig. 8B).

DISCUSSION

Viral proteins contribute to different aspects of disease outcome and pathogenesis during the course of viral infections (20, 30, 31). Reverse-genetics systems allow for the deletion of viral proteins to gain insight into their contribution to viral replication, pathogenesis, transmission, and/or disease outcome, among other things (34–37). We recently established a state-of-the-art reverse-genetics system for the efficient rescue of rSARS-CoV-2/WT (21, 22), which we used to generate ΔORF rSARS-CoV-2s and interrogate the contribution of the ORF3a, ORF6, ORF7a, ORF7b, and ORF8 accessory proteins in viral replication *in vitro* and *in vivo*. Similar studies have provided insight into

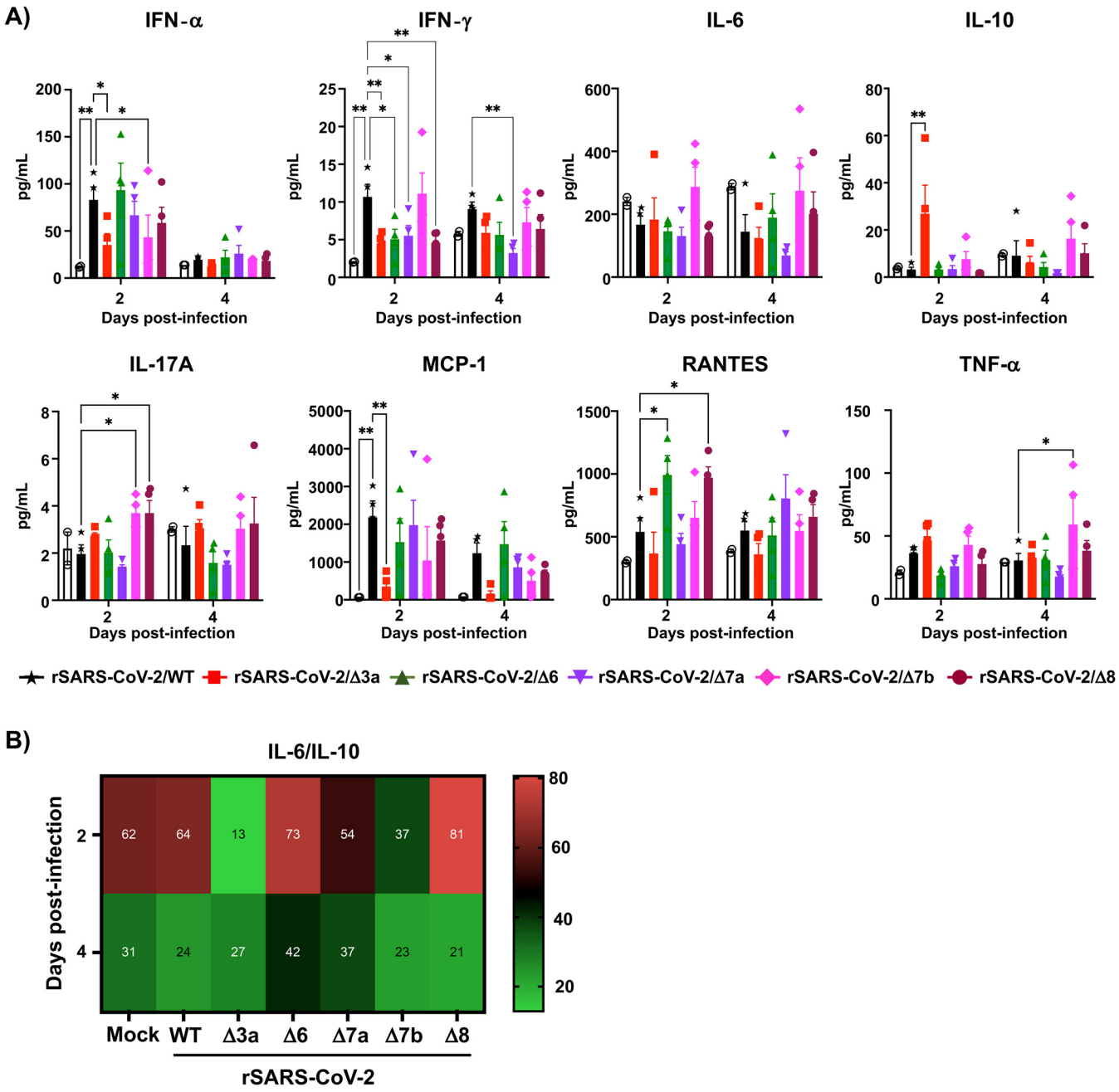

FIG 8 (A) The cytokine and chemokine storms in the lungs of K18 hACE2 transgenic mice mock infected and infected with the WT or a ΔORF rSARS-CoV-2 were determined using an 8-plex panel mouse ProcartaPlex assay. (B) The IL-6/IL-10 ratio as a marker of the local cytokine storm induced by rSARS-CoV-2 was determined. A two-way ANOVA of K18 hACE2 transgenic mice mock infected or infected with the WT or an ORF-deficient rSARS-CoV-2 was carried out with 4 mice per time point, except for the mock-infected group ($n = 2$).

the contribution of accessory ORF proteins in SARS-CoV infection *in vitro* and have identified a variety of functions, ranging from inhibition of host immune responses to activation of host cell death pathways (12–14, 17, 32, 34, 38–40). However, to date, no study has provided insight into the role of SARS-CoV-2 ORF accessory proteins in viral replication *in vitro* and/or in pathogenesis *in vivo*. Our study using robust genetic systems and the validated K18 hACE2 transgenic mouse model of SARS-CoV-2 infection provides us with useful information on the contribution of SARS-CoV-2 ORF3a, −6, −7a, −7b, and −8 accessory proteins to viral pathogenesis.

In this study, we generated rSARS-CoV-2 constructs deficient in the ORF3a, −6, −7a, −7b, or −8 accessory protein (Fig. 1) and characterized them both *in vitro* (Fig. 2

and 4) and *in vivo* (Fig. 5 and 8). Importantly, we were able to demonstrate the ORF-deficient nature of these rSARS-CoV-2s (Fig. 2 and 3). During our initial *in vitro* characterization, we first identified that ORF proteins contributed to early dissemination and formation of detectable viral plaques in Vero E6 cell monolayers; viruses lacking the ORF3a, −7a, −7b, and −8 proteins developed smaller plaques than rSARS-CoV-2/WT (Fig. 4). This was a surprising finding, as we observed only an ~1-$\log_{10}$ difference in growth kinetics between the WT and any of the ΔORF rSARS-CoV-2s (Fig. 4). Additionally, the variation in plaque morphology and size was indicative of ORF deletions having an impact on viral dissemination and fitness. This is turn correlates with other studies that have correlated plaque size phenotype and size with virulence and viral fitness (23–25).

To further determine the contribution of each ORF accessory protein in SARS-CoV-2 pathogenesis, we used our recently established K18 hACE2 transgenic mouse model (Fig. 5) (22). This particular *in vivo* study is the first, to our knowledge, that analyzes the contribution of SARS-CoV-2 ORF accessory proteins in viral infection in a validated animal model of infection. We observed a broad range of morbidity and survival outcomes between each of the ΔORF rSARS-CoV-2s and rSARS-CoV-2/WT (Fig. 5). SARS-CoV-2 ORF accessory proteins are encoded in the following order: ORF3a, −6, −7a, −7b, and −8. Our data collectively showed the greatest survival in mice infected with ORFΔ3a rSARS-CoV-2 (75%) and 100% mortality with ORFΔ8 rSARS-CoV-2. In this regard, a natural SARS-CoV-2 variant with a deletion of ORF8 has recently been isolated from patients presenting with COVID-19 symptoms (20). Thus, our results with ORFΔ8 rSARS-CoV-2 in the K18 hACE2 transgenic mouse model correspond to those observed in people infected with a natural ORFΔ8 SARS-CoV-2 isolate (20). Our findings with ORFΔ3a and ORFΔ6 rSARS-CoV-2s warrant further characterization, as there is limited insight into mechanistic exploitation of host pathways by ORF3a (12, 13, 32, 38, 39). Since it is well known that SARS-CoV-2 ORF6 is a potent inhibitor of the host innate immune response (11, 31), we were expecting low viral loads and an increased immune response with ΔORF6 rSARS-CoV-2; however, since SARS-CoV N protein also inhibits host immune responses (15, 41), it is plausible that SARS-CoV-2 N protein may have a function similar to that of OFR6 and may be responsible for counteracting host innate immune and inflammatory responses. An increase in immune responses may in turn correlate with the decrease in weight loss and recovery in the mice infected with ΔORF6 rSARS-CoV-2. Our chemokine and cytokine analysis indicates that, specifically, ORF3a is implicated in driving the host immune response to SARS-CoV-2 during the early stages of infection. Indeed, in the absence of ORF3a, we observed a general decrease of the cytokine storm (IL-6/IL-10 ratio), especially at 2 days p.i., when significantly decreased viral titers and tissue damage were also observed in the lungs of animals infected with ΔORF3a rSARS-CoV-2. Mechanistic studies of innate and adaptive immune responses, as well as modulation of IFN secretion, ion signaling channels, and cellular apoptotic and/or necrosis pathways, are important in determining the contributions of these ORF accessory proteins in viral pathogenesis *in vivo*. This is currently the focus of our ongoing *in vivo* studies with these ΔORF rSARS-CoV-2s. Overall, as with what was described with rSARS-CoV, our study highlights the findings that SARS-CoV ORF3a, −3b, −6, −7a, and −7b had no significant impact on viral replication *in vivo* (34) but that ORF3a seems to be involved in virulence, as its absence decreases SARS-CoV-2 virulence.

Overall, this study demonstrates the robustness of our BAC-based reverse-genetics approach to generate rSARS-CoV-2s, including those with deletions of ORF accessory proteins, and provides information on the contributions of ORF3a, −6, −7a, −7b, and −8 accessory proteins in viral fitness *in vitro* (Vero E6 cells) and *in vivo* in our recently established K18 hACE2 transgenic mouse model of SARS-CoV-2 infection and COVID-19 disease (22). Importantly, information from this study also provides novel insights for the generation of attenuated forms of SARS-CoV-2 for the development of live

attenuated vaccines for the treatment of this important respiratory pathogen and its associated COVID-19 disease.

MATERIALS AND METHODS

Biosafety. All the *in vitro* and *in vivo* experiments with an infectious natural isolate and rSARS-CoV-2 were conducted at appropriate biosafety level 3 (BSL3) and animal BSL3 (ABSL3) laboratories, respectively, at the Texas Biomedical Research Institute. Experiments were approved by the Texas Biomed Institutional Biosafety Committee (IBC) and Institutional Animal Care and Use Committee (IACUC).

Cells. African green monkey kidney epithelial cells (Vero E6, CRL-1586) were obtained from the American Type Culture Collection (ATCC; Bethesda, MD). The human embryonic kidney 293T (HEK293T) and the human lung carcinoma (A549) cell lines stably expressing hACE2 (hACE2-HEK293T and hACE2-A549, respectively) were obtained from BEI Resources (NR-52511 and NR-53821, respectively). All cell lines were maintained in Dulbecco's modified Eagle medium (DMEM) supplemented with 5% (vol/vol) fetal bovine serum (FBS; VWR) and 100 units/ml penicillin-streptomycin (Corning).

Reverse-genetics system. The BAC harboring the entire viral genome of SARS-CoV-2 USA-WA1/2020 (GenBank accession no. MN985325) was described previously (21). Deletion of individual accessory ORF proteins was achieved in viral fragment 1 by using inverse PCR and primer pairs containing a BsaI type IIS restriction endonuclease site. All the primer sequences are available upon request. Fragments, including those with individual deletions of accessory ORF proteins, were reassembled into the BAC using BamHI and RsrII restriction endonucleases.

Rescue of ΔORF rSARS-CoV-2s. Virus rescues were performed as previously described (21). Briefly, confluent monolayers of Vero E6 cells (10^6 cells/well, 6-well plates, triplicates) were transfected with 4.0 μg/well of the SARS-CoV-2 BAC using Lipofectamine 2000. After 24 h, transfection medium was exchanged for p.i. medium (DMEM supplemented with 2% [vol/vol] FBS), and cells were split and seeded into T75 flasks 48 h posttransfection. After incubation for another 72 h, tissue culture supernatants were collected, labeled as P0, and stored at −80°C. After viral titration of the supernatant, the P0 virus was used to infect fresh Vero E6 cells at a multiplicity of infection (MOI) of 0.0001 to make new viral stocks. Tissue culture supernatants were collected 72 h p.i., aliquoted, labeled as P1, and stored at −80°C for future use. To sequence the viral stocks, viral RNA was purified using the Direct-zol RNA MiniPrep Plus (Zymo) kit according to the manufacturer's instructions. Whole-genome amplification and sequencing were performed as previously described (42).

Immunofluorescence assay (IFA). Vero E6 cells (10^5 cells/well, 24-well plate format, triplicates) were mock infected or infected (MOI of 3) with the WT or a ΔORF rSARS-CoV-2. At 24 h p.i., cells were fixed with 10% formaldehyde solution at 4°C overnight and permeabilized using 0.5% (vol/vol) Triton X-100 in PBS for 15 min at room temperature. Cells were incubated overnight with 1 μg/ml of a SARS-CoV N protein cross-reactive polyclonal antibody at 4°C and a SARS-CoV-2 spike (S) cross-reactive monoclonal antibody (3B4), washed with PBS, and stained with a fluorescein isothiocyanate (FITC)-labeled goat anti-mouse IgG (1:200) and rhodamine-labeled goat anti-rabbit IgG (1:200). Nuclei were visualized by DAPI (4′,6-diamidino-2-phenylindole) staining. After being washed with PBS, cells were visualized and imaged with an EVOS microscope (ThermoFisher Scientific).

Plaque assay and immunostaining. Confluent monolayers of Vero E6 cells (10^6 cells/well, 6-well plate format, triplicates) were infected with serially diluted viruses for 1 h at 37°C. After viral adsorption, cells were overlaid with p.i. medium containing 1% low-melting-point agar and incubated at 37°C. At 72 h p.i., cells were fixed overnight with 10% formaldehyde solution. For immunostaining, cells were permeabilized with 0.5% (vol/vol) Triton X-100 in PBS for 15 min at room temperature and immunostained using the SARS-CoV N protein cross-reactive monoclonal antibody 1C7C7 (1 μg/ml) and the Vectastain ABC kit (Vector Laboratories) by following the manufacturers' instructions. After the immunostaining, plates were visualized on a ChemiDoc imager (Bio-Rad). Viral plaque diameters were measured with a standard ruler in centimeters.

Virus growth kinetics. Confluent monolayers of Vero E6 cells (10^6 cells/well, 6-well plate format, triplicates) were infected (MOI of 0.01) with the WT or a ΔORF rSARS-CoV-2. After 1 h of virus adsorption at 37°C, cells were washed with PBS and incubated in p.i. medium at 37°C. At the indicated times after infection, viral titers in tissue culture supernatants were determined by plaque assay and immunostaining using the SARS-CoV N protein cross-reactive monoclonal antibody 1C7C7, as previously described (43).

RT-PCR. Total RNA from Vero E6 cells (10^6 cells/well, 6-well plate format) infected (MOI of 0.01) with the WT or a ΔORF rSARS-CoV-2 was extracted with TRIzol reagent (Thermo Fisher Scientific) according to the manufacturer's instructions. Reverse transcription-PCR (RT-PCR) amplification was performed using SuperScript II reverse transcriptase (Thermo Fisher Scientific) and an expanded high-fidelity PCR system (Sigma-Aldrich). The amplified DNA products were subjected to 0.7% agarose gel analysis, and the gel-purified PCR fragments were subjected to Sanger sequencing (ACGT). All primer sequences used for RT-PCR are available upon request. Methods for Illumina library preparation, sequencing, and analysis of recombinant viruses followed those previously described (21).

Mice. Four- to 8-week-old specific-pathogen-free female B6.Cg-Tg(K18-ACE2)2Prlmn/J (stock no. 034860) K18 hACE2 transgenic mice were purchased from The Jackson Laboratory (Bar Harbor, ME). Our previous studies did not show significant sex-dependent differences in morbidity, mortality, or viral titers (22). K18 hACE2 transgenic mice were maintained in microisolator cages at ABSL3, provided sterile water and chow *ad libitum*, and acclimatized for 1 week prior to experimental manipulation. For morbidity and mortality studies, a total of 20 females were used ($n = 4$/group), whereas a total of 40 female mice ($n = 4$

per group) were used to determine viral titers at 2 and 4 days p.i. For the mock-infected control groups in the morbidity and mortality studies, 2 female K18 hACE2 transgenic mice were used and a total of 4 ($n = 2$ per time point) were used as mock-infected controls for gross pathology analysis.

Mouse infection and sample processing. K18 hACE2 transgenic mice were either mock (PBS) infected or infected intranasally (i.n.) with 10^5 PFU of the WT or a ΔORF rSARS-CoV-2 in a final volume of 50 μl following isoflurane sedation. After viral infection, mice were monitored daily for 14 days for morbidity (body weight loss) and mortality (survival). Mice showing >25% loss of their initial body weight were defined as reaching the experimental endpoint and humanely euthanized. For viral titers and gross pathology analysis, K18 hACE2 transgenic mice were infected as described above but euthanized at 2 or 4 days p.i. Nasal turbinates and lung tissues were harvested and homogenized in 1 ml of PBS using a Precellys tissue homogenizer (Bertin Instruments) for viral titrations. Tissue homogenates were centrifuged at 21,500 × g for 5 min, and supernatants were collected for determination of viral titer.

Multiplex cytokine assay. Multiple cytokines and chemokines (IFN-α, IFN-γ, IL-10, IL-17A, IL-6, MCP-1 or CCL2, RANTES or CCL5, TNF-α) were measured using a custom 8-plex panel mouse ProcartaPlex assay (ThermoFisher Scientific; catalog no. PPX-08-MXGZGFX, lot 279751-000) by following the manufacturer's instructions. An immunoassay was performed in the ABSL3 laboratory, and samples were decontaminated by an overnight incubation in 1% formaldehyde solution before readout on a Luminex 100/200 system running on xPONENT v4.2 with the following parameters: gate, 5,000 to 25,000; 50 μl of sample volume; 50 to 100 events per bead; sample timeout, 120 s; and low photomultiplier tube (PMT) (LMX100/200 default). Acquired data were analyzed using ProcartaPlex Analysis software v1.0.

Statistical analysis. Statistical analysis was performed using GraphPad Prism 8.3. For multiple comparisons, a 2-way analysis of variance (ANOVA) with multiple comparisons was performed.

ACKNOWLEDGMENTS

We thank Thomas Moran at the Icahn School of Medicine at Mount Sinai for providing us with the SARS-CoV cross-reactive N monoclonal antibody 1C7C7. We also thank BEI Resources for providing the SARS-CoV-2 USA-WA1/2020 isolate (NR-52281) and the hACE2-HEK293T (NR-52511) and hACE2-A549 (NR-53821) cell lines. Finally, we thank members at our institutes for their efforts in keeping them fully operational during the COVID-19 pandemic and the BSC and IACUC committees for reviewing our protocols in a time-efficient manner.

This work was partly funded by the Center for Research for Influenza Pathogenesis (CRIP), a NIAID supported Center of Excellence for Influenza Research and Surveillance (CEIRS; contract number HHSN272201400008C), by the Defense Advanced Research Projects Agency (HR0011-19-2-0020), and by the generous support of the JPB Foundation, the Open Philanthropy Project (research grant 2020-215611 (5384), and anonymous donors to A.G.-S.

REFERENCES

1. Cui J, Li F, Shi ZL. 2019. Origin and evolution of pathogenic coronaviruses. Nat Rev Microbiol 17:181–192. https://doi.org/10.1038/s41579-018-0118-9.
2. de Wit E, van Doremalen N, Falzarano D, Munster VJ. 2016. SARS and MERS: recent insights into emerging coronaviruses. Nat Rev Microbiol 14:523–534. https://doi.org/10.1038/nrmicro.2016.81.
3. Woo PC, Lau SK, Lam CS, Lau CC, Tsang AK, Lau JH, Bai R, Teng JL, Tsang CC, Wang M, Zheng BJ, Chan KH, Yuen KY. 2012. Discovery of seven novel mammalian and avian coronaviruses in the genus deltacoronavirus supports bat coronaviruses as the gene source of alphacoronavirus and betacoronavirus and avian coronaviruses as the gene source of gammacoronavirus and deltacoronavirus. J Virol 86:3995–4008. https://doi.org/10.1128/JVI.06540-11.
4. Haagmans BL, Al Dhahiry SH, Reusken CB, Raj VS, Galiano M, Myers R, Godeke GJ, Jonges M, Farag E, Diab A, Ghobashy H, Alhajri F, Al-Thani M, Al-Marri SA, Al Romaihi HE, Al Khal A, Bermingham A, Osterhaus AD, AlHajri MM, Koopmans MP. 2014. Middle East respiratory syndrome coronavirus in dromedary camels: an outbreak investigation. Lancet Infect Dis 14:140–145. https://doi.org/10.1016/S1473-3099(13)70690-X.
5. Luk HKH, Li X, Fung J, Lau SKP, Woo PCY. 2019. Molecular epidemiology, evolution and phylogeny of SARS coronavirus. Infect Genet Evol 71:21–30. https://doi.org/10.1016/j.meegid.2019.03.001.
6. López-Ortiz E, López-Ortiz G, Mendiola-Pastrana IR, Mazón-Ramírez JJ, Díaz-Quiñonez JA. 2020. From the handling of an outbreak by an unknown pathogen in Wuhan to the preparedness and response in the face of the emergence of Covid-19 in Mexico. Gac Med Mex 156:132–137. https://doi.org/10.24875/GMM.M20000346.
7. Ralph R, Lew J, Zeng T, Francis M, Xue B, Roux M, Toloue Ostadgavahi A, Rubino S, Dawe NJ, Al-Ahdal MN, Kelvin DJ, Richardson CD, Kindrachuk J, Falzarano D, Kelvin AA. 2020. 2019-nCoV (Wuhan virus), a novel coronavirus: human-to-human transmission, travel-related cases, and vaccine readiness. J Infect Dev Ctries 14:3–17. https://doi.org/10.3855/jidc.12425.
8. Malik YA. 2020. Properties of coronavirus and SARS-CoV-2. Malays J Pathol 42:3–11.
9. Fernandes JD, Hinrichs AS, Clawson H, Gonzalez JN, Lee BT, Nassar LR, Raney BJ, Rosenbloom KR, Nerli S, Rao AA, Schmelter D, Fyfe A, Maulding N, Zweig AS, Lowe TM, Ares M, Corbet-Detig R, Kent WJ, Haussler D, Haeussler M. 2020. The UCSC SARS-CoV-2 Genome Browser. Nat Genet 52:991–998. https://doi.org/10.1038/s41588-020-0700-8.
10. Yuan S, Peng L, Park JJ, Hu Y, Devarkar SC, Dong MB, Shen Q, Wu S, Chen S, Lomakin IB, Xiong Y. 2020. Nonstructural protein 1 of SARS-CoV-2 is a potent pathogenicity factor redirecting host protein synthesis machinery toward viral RNA. Mol Cell 80:1055–1066.e6. https://doi.org/10.1016/j.molcel.2020.10.034.
11. Lei X, Dong X, Ma R, Wang W, Xiao X, Tian Z, Wang C, Wang Y, Li L, Ren L, Guo F, Zhao Z, Zhou Z, Xiang Z, Wang J. 2020. Activation and evasion of type I interferon responses by SARS-CoV-2. Nat Commun 11:3810. https://doi.org/10.1038/s41467-020-17665-9.
12. Issa E, Merhi G, Panossian B, Salloum T, Tokajian S. 2020. SARS-CoV-2 and ORF3a: nonsynonymous mutations, functional domains, and viral pathogenesis. mSystems 5:e00266-20. https://doi.org/10.1128/mSystems.00266-20.
13. Ren Y, Shu T, Wu D, Mu J, Wang C, Huang M, Han Y, Zhang XY, Zhou W, Qiu Y, Zhou X. 2020. The ORF3a protein of SARS-CoV-2 induces apoptosis in cells. Cell Mol Immunol 17:881–883. https://doi.org/10.1038/s41423-020-0485-9.

14. Freundt EC, Yu L, Goldsmith CS, Welsh S, Cheng A, Yount B, Liu W, Frieman MB, Buchholz UJ, Screaton GR, Lippincott-Schwartz J, Zaki SR, Xu XN, Baric RS, Subbarao K, Lenardo MJ. 2010. The open reading frame 3a protein of severe acute respiratory syndrome-associated coronavirus promotes membrane rearrangement and cell death. J Virol 84:1097–1109. https://doi.org/10.1128/JVI.01662-09.
15. Kopecky-Bromberg SA, Martínez-Sobrido L, Frieman M, Baric RA, Palese P. 2007. Severe acute respiratory syndrome coronavirus open reading frame (ORF) 3b, ORF 6, and nucleocapsid proteins function as interferon antagonists. J Virol 81:548–557. https://doi.org/10.1128/JVI.01782-06.
16. Kopecky-Bromberg SA, Martinez-Sobrido L, Palese P. 2006. 7a protein of severe acute respiratory syndrome coronavirus inhibits cellular protein synthesis and activates p38 mitogen-activated protein kinase. J Virol 80:785–793. https://doi.org/10.1128/JVI.80.2.785-793.2006.
17. Schaecher SR, Mackenzie JM, Pekosz A. 2007. The ORF7b protein of severe acute respiratory syndrome coronavirus (SARS-CoV) is expressed in virus-infected cells and incorporated into SARS-CoV particles. J Virol 81:718–731. https://doi.org/10.1128/JVI.01691-06.
18. Schaecher SR, Diamond MS, Pekosz A. 2008. The transmembrane domain of the severe acute respiratory syndrome coronavirus ORF7b protein is necessary and sufficient for its retention in the Golgi complex. J Virol 82:9477–9491. https://doi.org/10.1128/JVI.00784-08.
19. Su YCF, Anderson DE, Young BE, Linster M, Zhu F, Jayakumar J, Zhuang Y, Kalimuddin S, Low JGH, Tan CW, Chia WN, Mak TM, Octavia S, Chavatte JM, Lee RTC, Pada S, Tan SY, Sun L, Yan GZ, Maurer-Stroh S, Mendenhall IH, Leo YS, Lye DC, Wang LF, Smith GJD. 2020. Discovery and genomic characterization of a 382-nucleotide deletion in ORF7b and ORF8 during the early evolution of SARS-CoV-2. mBio 11:e01610-20. https://doi.org/10.1128/mBio.01610-20.
20. Young BE, Fong SW, Chan YH, Mak TM, Ang LW, Anderson DE, Lee CY, Amrun SN, Lee B, Goh YS, Su YCF, Wei WE, Kalimuddin S, Chai LYA, Pada S, Tan SY, Sun L, Parthasarathy P, Chen YYC, Barkham T, Lin RTP, Maurer-Stroh S, Leo YS, Wang LF, Renia L, Lee VJ, Smith GJD, Lye DC, Ng LFP. 2020. Effects of a major deletion in the SARS-CoV-2 genome on the severity of infection and the inflammatory response: an observational cohort study. Lancet 396:603–611. https://doi.org/10.1016/S0140-6736(20)31757-8.
21. Ye C, Chiem K, Park JG, Oladunni F, Platt RN, II, Anderson T, Almazan F, de la Torre JC, Martinez-Sobrido L. 2020. Rescue of SARS-CoV-2 from a single bacterial artificial chromosome. mBio 11:e02168-20. https://doi.org/10.1128/mBio.02168-20.
22. Oladunni FS, Park JG, Pino PA, Gonzalez O, Akhter A, Allué-Guardia A, Olmo-Fontánez A, Gautam S, Garcia-Vilanova A, Ye C, Chiem K, Headley C, Dwivedi V, Parodi LM, Alfson KJ, Staples HM, Schami A, Garcia JI, Whigham A, Platt RN, Gazi M, Martinez J, Chuba C, Earley S, Rodriguez OH, Mdaki SD, Kavelish KN, Escalona R, Hallam CRA, Christie C, Patterson JL, Anderson TJC, Carrion R, Dick EJ, Hall-Ursone S, Schlesinger LS, Alvarez X, Kaushal D, Giavedoni LD, Turner J, Martinez-Sobrido L, Torrelles JB. 2020. Lethality of SARS-CoV-2 infection in K18 human angiotensin-converting enzyme 2 transgenic mice. Nat Commun 11:6122. https://doi.org/10.1038/s41467-020-19891-7.
23. Kato F, Tajima S, Nakayama E, Kawai Y, Taniguchi S, Shibasaki K, Taira M, Maeki T, Lim CK, Takasaki T, Saijo M. 2017. Characterization of large and small-plaque variants in the Zika virus clinical isolate ZIKV/Hu/S36/Chiba/2016. Sci Rep 7:16160. https://doi.org/10.1038/s41598-017-16475-2.
24. Kim YI, Murphy R, Majumdar S, Harrison LG, Aitken J, DeVincenzo JP. 2015. Relating plaque morphology to respiratory syncytial virus subgroup, viral load, and disease severity in children. Pediatr Res 78:380–388. https://doi.org/10.1038/pr.2015.122.
25. Goh KC, Tang CK, Norton DC, Gan ES, Tan HC, Sun B, Syenina A, Yousuf A, Ong XM, Kamaraj US, Cheung YB, Gubler DJ, Davidson A, St John AL, Sessions OM, Ooi EE. 2016. Molecular determinants of plaque size as an indicator of dengue virus attenuation. Sci Rep 6:26100. https://doi.org/10.1038/srep26100.
26. Jureka AS, Silvas JA, Basler CF. 2020. Propagation, inactivation, and safety testing of SARS-CoV-2. Viruses 12:622. https://doi.org/10.3390/v12060622.
27. Case JB, Bailey AL, Kim AS, Chen RE, Diamond MS. 2020. Growth, detection, quantification, and inactivation of SARS-CoV-2. Virology 548:39–48. https://doi.org/10.1016/j.virol.2020.05.015.
28. Wang Q, Zhang Y, Wu L, Niu S, Song C, Zhang Z, Lu G, Qiao C, Hu Y, Yuen KY, Wang Q, Zhou H, Yan J, Qi J. 2020. Structural and functional basis of SARS-CoV-2 entry by using human ACE2. Cell 181:894–904.e9. https://doi.org/10.1016/j.cell.2020.03.045.
29. Stukalov A, Girault V, Grass V, Karayel O, Bergant V, Urban C, Haas DA, Huang Y, Oubraham L, Wang A, Hamad MS, Piras A, Hansen FM, Tanzer MC, Paron I, Zinzula L, Engleitner T, Reinecke M, Lavacca TM, Ehmann R, Wolfel R, Jores J, Kuster B, Protzer U, Rad R, Ziebuhr J, Thiel V, Scaturro P, Mann M, Pichlmair A. 2021. Multilevel proteomics reveals host perturbations by SARS-CoV-2 and SARS-CoV. Nature 594:246–252. https://doi.org/10.1038/s41586-021-03493-4.
30. Shi CS, Nabar NR, Huang NN, Kehrl JH. 2019. SARS-coronavirus open reading frame-8b triggers intracellular stress pathways and activates NLRP3 inflammasomes. Cell Death Discov 5:101. https://doi.org/10.1038/s41420-019-0181-7.
31. Yuen CK, Lam JY, Wong WM, Mak LF, Wang X, Chu H, Cai JP, Jin DY, To KK, Chan JF, Yuen KY, Kok KH. 2020. SARS-CoV-2 nsp13, nsp14, nsp15 and orf6 function as potent interferon antagonists. Emerg Microbes Infect 9:1418–1428. https://doi.org/10.1080/22221751.2020.1780953.
32. Majumdar P, Niyogi S. 2020. ORF3a mutation associated with higher mortality rate in SARS-CoV-2 infection. Epidemiol Infect 148:e262. https://doi.org/10.1017/S0950268820002599.
33. Dhar SK, K V, Damodar S, Gujar S, Das M. 2021. IL-6 and IL-10 as predictors of disease severity in COVID-19 patients: results from meta-analysis and regression. Heliyon 7:e06155. https://doi.org/10.1016/j.heliyon.2021.e06155.
34. Yount B, Roberts RS, Sims AC, Deming D, Frieman MB, Sparks J, Denison MR, Davis N, Baric RS. 2005. Severe acute respiratory syndrome coronavirus group-specific open reading frames encode nonessential functions for replication in cell cultures and mice. J Virol 79:14909–14922. https://doi.org/10.1128/JVI.79.23.14909-14922.2005.
35. Kalveram B, Lihoradova O, Indran SV, Ikegami T. 2011. Using reverse genetics to manipulate the NSs gene of the Rift Valley fever virus MP-12 strain to improve vaccine safety and efficacy. J Vis Exp 2011:e3400. https://doi.org/10.3791/3400.
36. Nishiyama S, Slack OA, Lokugamage N, Hill TE, Juelich TL, Zhang L, Smith JK, Perez D, Gong B, Freiberg AN, Ikegami T. 2016. Attenuation of pathogenic Rift Valley fever virus strain through the chimeric S-segment encoding sandfly fever phlebovirus NSs or a dominant-negative PKR. Virulence 7:871–881. https://doi.org/10.1080/21505594.2016.1195528.
37. Theriault S, Groseth A, Artsob H, Feldmann H. 2005. The role of reverse genetics systems in determining filovirus pathogenicity. Arch Virol Suppl 2005:157–177. https://doi.org/10.1007/3-211-29981-5_13:157-77.
38. Bianchi M, Borsetti A, Ciccozzi M, Pascarella S. 2021. SARS-Cov-2 ORF3a: mutability and function. Int J Biol Macromol 170:820–826. https://doi.org/10.1016/j.ijbiomac.2020.12.142.
39. Miao G, Zhao H, Li Y, Ji M, Chen Y, Shi Y, Bi Y, Wang P, Zhang H. 2021. ORF3a of the COVID-19 virus SARS-CoV-2 blocks HOPS complex-mediated assembly of the SNARE complex required for autolysosome formation. Dev Cell 56:427–442.e5. https://doi.org/10.1016/j.devcel.2020.12.010.
40. Siu KL, Yuen KS, Castaño-Rodriguez C, Ye ZW, Yeung ML, Fung SY, Yuan S, Chan CP, Yuen KY, Enjuanes L, Jin DY. 2019. Severe acute respiratory syndrome coronavirus ORF3a protein activates the NLRP3 inflammasome by promoting TRAF3-dependent ubiquitination of ASC. FASEB J 33:8865–8877. https://doi.org/10.1096/fj.201802418R.
41. Hu Y, Li W, Gao T, Cui Y, Jin Y, Li P, Ma Q, Liu X, Cao C. 2017. The severe acute respiratory syndrome coronavirus nucleocapsid inhibits type I interferon production by interfering with TRIM25-mediated RIG-I ubiquitination. J Virol 91:e02143-16. https://doi.org/10.1128/JVI.02143-16.
42. Gonzalez-Reiche AS, Hernandez MM, Sullivan MJ, Ciferri B, Alshammary H, Obla A, Fabre S, Kleiner G, Polanco J, Khan Z, Alburquerque B, van de Guchte A, Dutta J, Francoeur N, Melo BS, Oussenko I, Deikus G, Soto J, Sridhar SH, Wang YC, Twyman K, Kasarskis A, Altman DR, Smith M, Sebra R, Aberg J, Krammer F, Garcia-Sastre A, Luksza M, Patel G, Paniz-Mondolfi A, Gitman M, Sordillo EM, Simon V, van Bakel H. 2020. Introductions and early spread of SARS-CoV-2 in the New York City area. Science 369:297–301. https://doi.org/10.1126/science.abc1917.
43. Chiem K, Morales Vasquez D, Park JG, Platt RN, Anderson T, Walter MR, Kobie JJ, Ye C, Martinez-Sobrido L. 2021. Generation and characterization of recombinant SARS-CoV-2 expressing reporter genes. J Virol 95:e02209-20. https://doi.org/10.1128/JVI.02209-20.